metals

MDPI

Article

Multi-Physics Analysis of Machining Ti-6Al-4V Alloy: Experimental Characterization and a New Material Behavior Modeling

Badis Haddag [1,*], Dominique Yameogo [2], Mohammed Nouari [1] and Hamid Makich [1]

[1] LEM3 Laboratory, UMR CNRS 7239 and Lorraine University, Institut Mines-Telecom (InSIC), 27 Voie de l'Innovation, 88100 Saint-Dié, France; mohammed.nouari@univ-lorraine.fr (M.N.); hamid.makich@univ-lorraine.fr (H.M.)
[2] Research Center, APERAM Alloys, Avenue Jean Jaurès, 58660 Imphy, France; dominique.yameogo@aperam.com
* Correspondence: badis.haddag@univ-lorraine.fr; Tel.: +33-(0)3-2942-2330

Abstract: Titanium alloys are considered difficult-to-cut materials due to their low machinability. Understanding the physical mechanisms occurring during cutting titanium alloys is of particular interest to improve their machinability. Experimental and numerical investigations on Ti-6Al-4V alloy machining are proposed in this paper. Orthogonal cutting tests are performed. The chip microstructure is characterized using SEM observations coupled with the EBSD technique to reveal the deformation mechanisms occurring inside the microstructure. Based on these microscale observations, a new hybrid flow stress model considering the link between the microstructure and damage evolutions is proposed. The model was implemented FE code to simulate the cutting process. The morphology of generated chips and microstructural parameters were deeply analyzed and compared with experimental data. The effect of the dynamic recrystallization phenomenon and its interaction with damage on the cutting process was discussed. The model can be applied for machining simulations of Ti-6Al-4V and other titanium alloys to better choose adequate cutting conditions.

Keywords: machining Ti-6Al-4V; cutting process; physical-based behavior; microstructure vs. damage; FE modeling

check for updates

Citation: Haddag, B.; Yameogo, D.; Nouari, M.; Makich, H. Multi-Physics Analysis of Machining Ti-6Al-4V Alloy: Experimental Characterization and a New Material Behavior Modeling. *Metals* **2022**, *12*, 581. https://doi.org/10.3390/met12040581

Academic Editors: Francesco Iacoviello, Umberto Prisco and Sergey N. Grigoriev

Received: 10 February 2022
Accepted: 24 March 2022
Published: 29 March 2022

Publisher's Note: MDPI stays neutral with regard to jurisdictional claims in published maps and institutional affiliations.

Copyright: © 2022 by the authors. Licensee MDPI, Basel, Switzerland. This article is an open access article distributed under the terms and conditions of the Creative Commons Attribution (CC BY) license (https://creativecommons.org/licenses/by/4.0/).

1. Introduction

Titanium alloys are suitable for advanced technology applications, such as aeronautical components, biomedical implants, and prostheses, due to their high tensile strength, low density, and good resistance to corrosion and temperature. Since titanium alloys are difficult-to-cut materials, this implies a high manufacturing cost. Several problems, such as premature tool wear [1], poor surface quality [2], or affected surface microstructure [3], are encountered during machining these alloys. In order to follow specific guidelines in order to achieve part quality when machining these materials, manufacturers use [4]: high quantity of cutting fluid, low cutting speed, maintaining sharp cutting tool edges, etc. However, these procedures induce high machining cost levels for titanium alloys than the other usual materials, such as steels with equivalent hardness. The study of the cutting material is an important step to optimize and improve the machining process. Most of the machining problems of titanium alloys are due to their behavior. For example, the elastic behavior of titanium during machining induces vibration due to the low material rigidity. Another machining problem concerns their thermal characteristics. Due to low thermal conductivity of titanium alloys, this induces temperature localization in the cutting zone. This leads to a premature tool wear by softening the active part of the cutting tool, and a damage in the machined part.

The analysis of chip formation is one way to understand the cutting process. For instance, the chip segmentation is related to many problems encountered when machining

Ti-6Al-4V, such as the cutting forces oscillation and the poor surface roughness. Sun et al. [1] studied the cutting of Ti-6Al-4V and obtained chips that were partially segmented and partially continuous. From the comparison of the segmentation frequency to the cutting force fluctuation frequency, it was concluded that fluctuations result from the chips segmentation process. The cyclic force peak due to segmentation was about 1.18 times higher than the static force caused by continuous chips. Therefore, it is important to estimate the chip segmentation frequency since it induces vibrations that can lead to the cutting tool deterioration (premature wear). Su et al. [5] investigated the effect of chip segmentation on the surface roughness and found that there is a strong correlation between geometrical parameters of the segmented chips and machined surface roughness.

In addition, several studies were conducted to understand the Ti-6Al-4V cutting and two physical mechanisms were largely observed and analyzed. The first one is the periodic fracture due to ductile damage mechanisms occurring in the chip. Nakayama [6] explained the saw-tooth chip formation by cyclic crack formation. The crack initiates at the chip-free surface where the hydrostatic pressure is zero and propagates during the chip formation. Umbrello [7] simulated Ti-6Al-4V chips with a 2D finite element model using Cockroft and Latham's damage criterion to produce this cyclic crack formation. A 3D finite element model that predicts chip segmentation, based on this crack initiation and propagation theory, was proposed by Aurich and Bil [8]. Recently, a fracture criterion considering the state of stress and strain-rate effects was proposed by Cheng et al. [9] and applied by Xu et al. [10] for machining simulation of Ti-6Al-4V. The fracture in the localize shear bands in the chip is not explicitly reproduced by their adopted model.

The second mechanism is characterized by the formation of adiabatic shear bands (ASB) due to severe plastic deformation. Segmented chips present a heterogeneous distribution of plastic strain, with areas where there is a strong localization of deformation (ASB) and undeformed areas. During the chip formation, observations with a high-speed camera [11] show that the ASB propagates from the tool tip toward the chip-free surface. The fast formation of the ASB by plastic shearing is often called catastrophic shearing. The formation of ASB was initially considered to be the consequence of the material thermal softening. Zhen-Bin and Komanduri [12] explained that the thermal softening effect becomes stronger than the material hardening in the primary shear zone, resulting in the formation of ASB and then the formation of the segmented chip. Davies et al. [13] proposed that competition between hardening and thermal softening happens, and segmented chips are formed when the cutting speed is too high and breaks the balance between heat diffusion and plastic deformation.

Recent investigations show that the ASB formation is related to microstructure transformation, namely phase transformation or dynamic recrystallization (DRX). Xue et al. [14] conducted shearing tests on cylindrical specimens of Ti-6Al-4V and examined the microstructure within the band. They observed microstructure changes and concluded that these were due to DRX. Grebe et al. [15] studied the ASB formation of Ti-6Al-4V using transmission microscopy and observed very fine grains with a size of about 0.3 µm. Wan et al. [16] confirm that by studying the microstructure of the Ti-6Al-4V ASB and also observed sub-micrometric grains due to DRX and phase transformation. Several papers [16–18] tend to associate the DRX to the softening and then to the chip formation during machining. Based on DRX observations, Rhim and Oh [17] proposed a flow stress model taking into account this microstructural transformation and simulated the AISI 1045 steel chip formation. Calamaz et al. [18] introduced for the first time the strain-softening phenomenon due to DRX in a numerical model named TANgent Hyperbolic (TANH) and simulated the chip segmentation when machining Ti-6Al-4V. Chen et al. [19] studied the microstructure evolution within ASB and observed grains refinement due to rotation dynamic recrystallization.

The link between microstructure transformation and damage in machining is also highlighted in the literature. Liu et al. [20] considered the contribution of damage and dynamic recovery during the chip formation process and proposed a modified Zerilli-Armstrong flow stress model. However, the damage can be affected by restoration phenomena, such

as recrystallization or recovery. Shang et al. [21] showed while studying the 316LN steel that DRX impedes void growth and coalescence. Since recrystallization is a restoration process, it restores the material ductility by reducing or limiting the damage mechanism. Hence, the effect of recrystallization occurrence on the damage evolution was particularly investigated here.

Therefore, the aim of this paper was to analyze the combined effect of microstructure transformation and damage in the Ti-6Al-4V alloy during the cutting process. Firstly, orthogonal cutting tests were performed. Then, based on the experimental characterization, a new model is proposed to reproduce the actual behavior of the work material during machining. Thus, the main contribution is the development of a microstructure-dependent damage model for a better prediction of the cutting process of Ti-6Al-4V alloy. The model can be used for machining other metals involving interaction between damage occurrence and microstructure change in the work material during machining.

2. Mechanisms of Machining Ti-6Al-4V

To analyze the mechanisms of cutting Ti-6Al-4V, orthogonal cutting tests under dry conditions were performed.

2.1. Experimental Tests

The initial workpiece of Ti-6Al-4V is a cylinder with disks prepared for orthogonal cutting tests on a horizontal CNC lathe (MAZAK 200M model, Oguchi, Japan). The initial diameter of each disk is about 70 mm, and the final diameter after machining is about 40 mm. The chemical composition of this material is reported in Table 1. The cutting inserts (provided by EVATEC-Tools, Thionville, France) are made of tungsten carbide with 6% of cobalt as a binder (WC–Co). The main geometric characteristics are as follows: rake angle of 0°, clearance angle of 7°, and a cutting-edge radius of about 30 µm.

Table 1. Chemical composition of the Ti-6Al-4V.

Al	V	C	Fe	H	W	O	Ti
6%	4%	≤0.08%	≤0.3	≤0.0125	≤0.07	≤0.2	Balance

Cutting conditions are a combination of three cutting speeds and three feed rates (see Table 2). The feed rate corresponds to the depth of cut in orthogonal turning. The cutting width is kept constant and equal to 3 mm. The ratio of this width on the depth of cut is higher than 3.5 for all tested cases to obtain orthogonal cutting with plane strain assumption [22]. The tool moves in an orthogonal direction to the revolution axis of the part. Therefore, the relative displacement between the tool and the part is in the plane defined by the feed direction and the cutting speed direction.

Table 2. Cutting conditions.

Test N°	V_c (m/min)	f (mm/rev)
1	25	0.075
2	100	
3	150	
4	25	0.18
5	100	
6	150	
7	25	0.35
8	100	
9	150	

2.2. Analysis of the Cutting Process

Various aspects of the cutting process can be analyzed in machining, such as tool wear, surface integrity, chip formation process, vibration, etc. In this study, the analysis was focused on the chip formation process. Indeed, the chips contain the main mechanisms occurring in the cutting zone (high localized deformation, abrupt increase in temperature, damage and fracture, microstructure change, etc.). Hence, generated chips were analyzed (i) qualitatively to highlight the transition from continuous to discontinuous chips, (ii) quantitatively to quantify the chips morphology with respect to cutting conditions, and (iii) at the microscale to reveal the mechanisms of microstructure change and damage induced by the cutting process.

2.2.1. Qualitative vs. Quantitative Analysis of Chips

The chips obtained from all orthogonal cutting tests were collected and analyzed. Figure 1 presents two typical chips. Chips segmentation occurred for all the cases. The low feed (0.075 mm/rev) induced aperiodic chips. A similar observation of chips was found for the test with f = 0.18 mm/rev and V_c = 25 m/min. The segmented chips appeared to be aperiodic for low cutting speed and feed or, in other words, for low material flow. This influence of the undeformed chip thickness on the chip morphology was also revealed by Ducobu et al. [22] for Ti-6Al-4V machining. Calamaz [11] also showed, in orthogonal cutting Ti-6Al-4V, an increase in the cutting speed or feed leads to an intensification of segmentation (augmentation of the segmentation frequency).

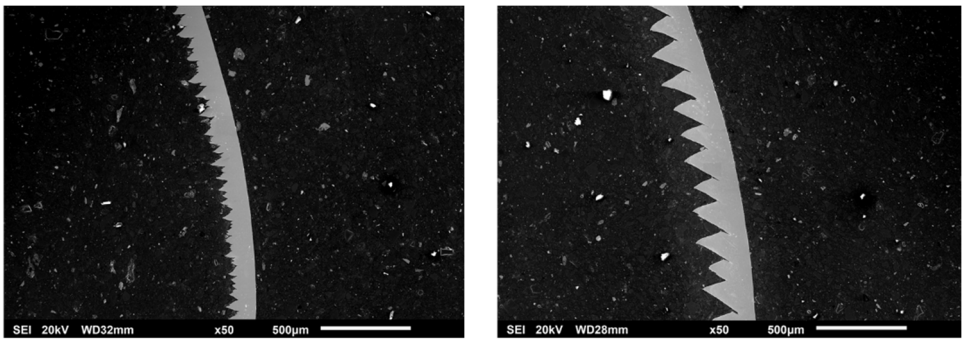
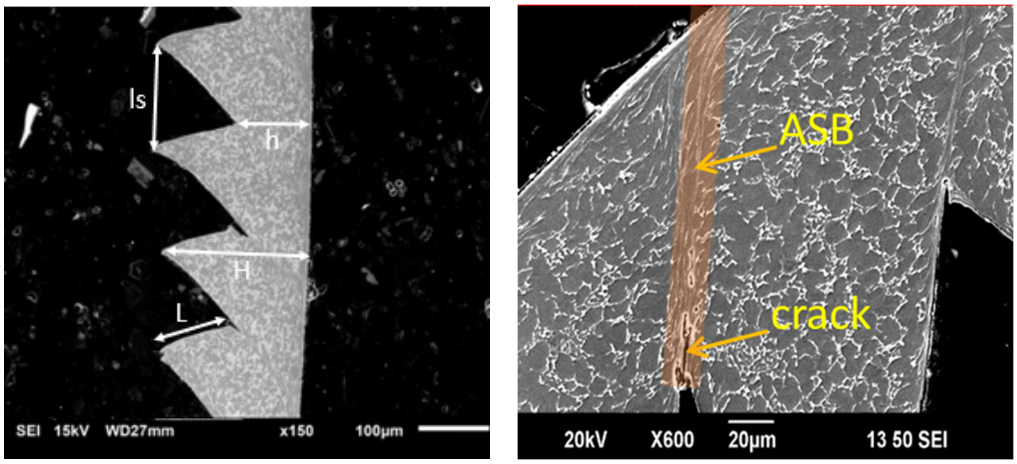


Figure 1. Ti-6Al-4V chip morphologies for two feed rates.

Quantitative analysis of chips morphology using adequate geometric parameters allows a more precise analysis (Atlati et al. [23], Kouadri et al. [24]). The basic parameters used to describe the chip morphology are H, h, L and l_S, shown in Figure 2a. H and h are the maximum and minimum deformed chip thickness, respectively; L is the deformed surface length; and l_S is the distance between two segments from peak to peak. Figure 2b clearly shows the formation of the ASB between two segments and the initiation of a microcrack at its extremity.

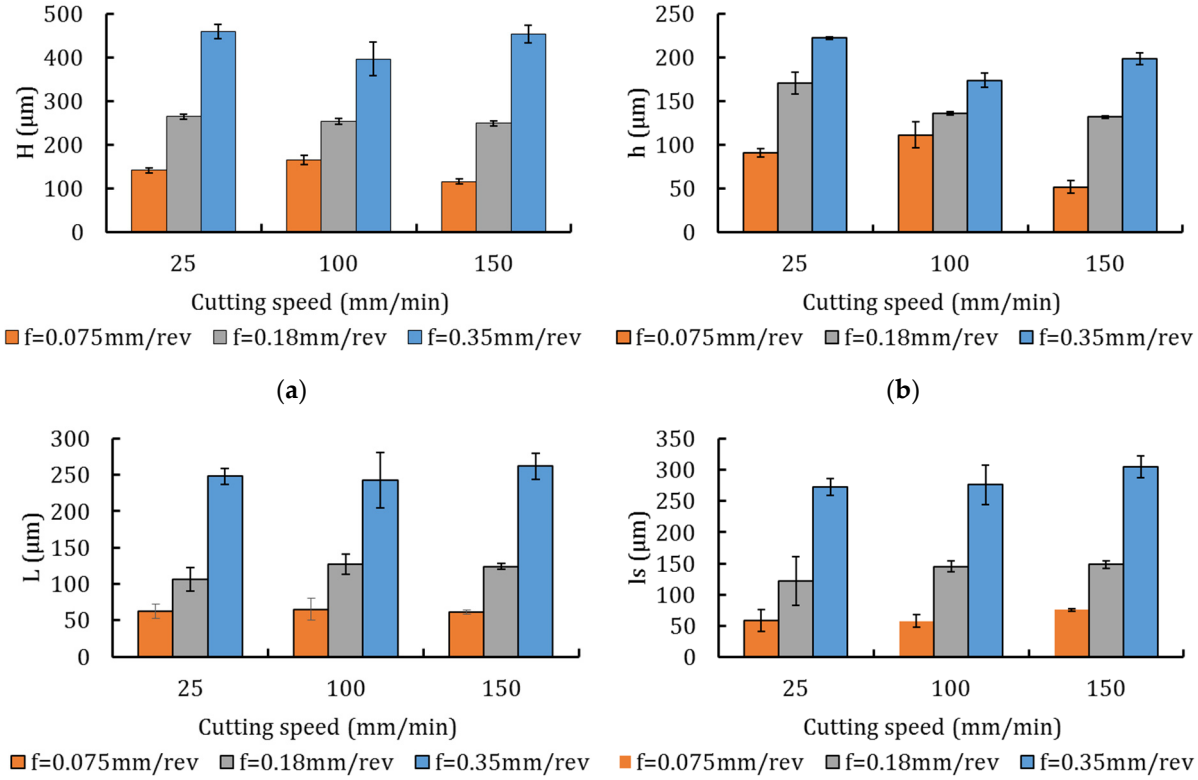
The measured chip morphology parameters are summarized in Figure 3. An increase in all parameters was observed as the feed was increased. The increase in cutting speed shows a little effect on H and h (Figure 3a,b), but a slight increase in L and l_S (Figure 3c,d), i.e., the segments are more spaced. This is not the case of the lowest feed, for which the chip segmentation is aperiodic. Irregular segments are formed, corresponding to variable geometry parameters along the chip. There is no clear trend (increase or decrease) of chip parameters as cutting speed increases. The complex interaction between the work-hardening (dominant at low V_c speeds) and work-softening (dominant at higher V_c), mainly in the formed localized shear bands, leads to such variations. In the next section,

more insight on the mechanism of chip formation (interaction of damage occurrence and microstructure change) is addressed.



(**a**) (**b**)

Figure 2. SEM micrographs of a typical chip: (**a**) chip morphology parameters (**b**) zoom on the chip showing the ASB between two segments and initiation of crack (V_c = 100 m/min, f = 0.18 mm/rev).



(**a**) (**b**)

(**c**) (**d**)

Figure 3. Measured chip morphology parameters for different cutting conditions.

In addition to these chip morphology parameters, chip compression ratios are often used to analyze the chip formation process further [24]. The chip compression ratio is a value giving an indication of the plastic deformation undergone by the chip. It is the ratio of the deformed chip thickness to the undeformed chip thickness. Since the segmented chip has a heterogeneous distribution of plastic strain, three values of the chip compression ratio

are calculated [24] and ploted in Figure 4: the minimum $CR_{\min}$ (Figure 4a), the maximum value $CR_{\max}$ (Figure 4b), and the mean value CR_{mean} (Figure 4c), defined by Equation (1).

$$CR_{\max} = \frac{H}{f}, CR_{\min} = \frac{h}{f}, CR_{\mathrm{mean}} = \frac{(H+h)}{2f} \quad (1)$$

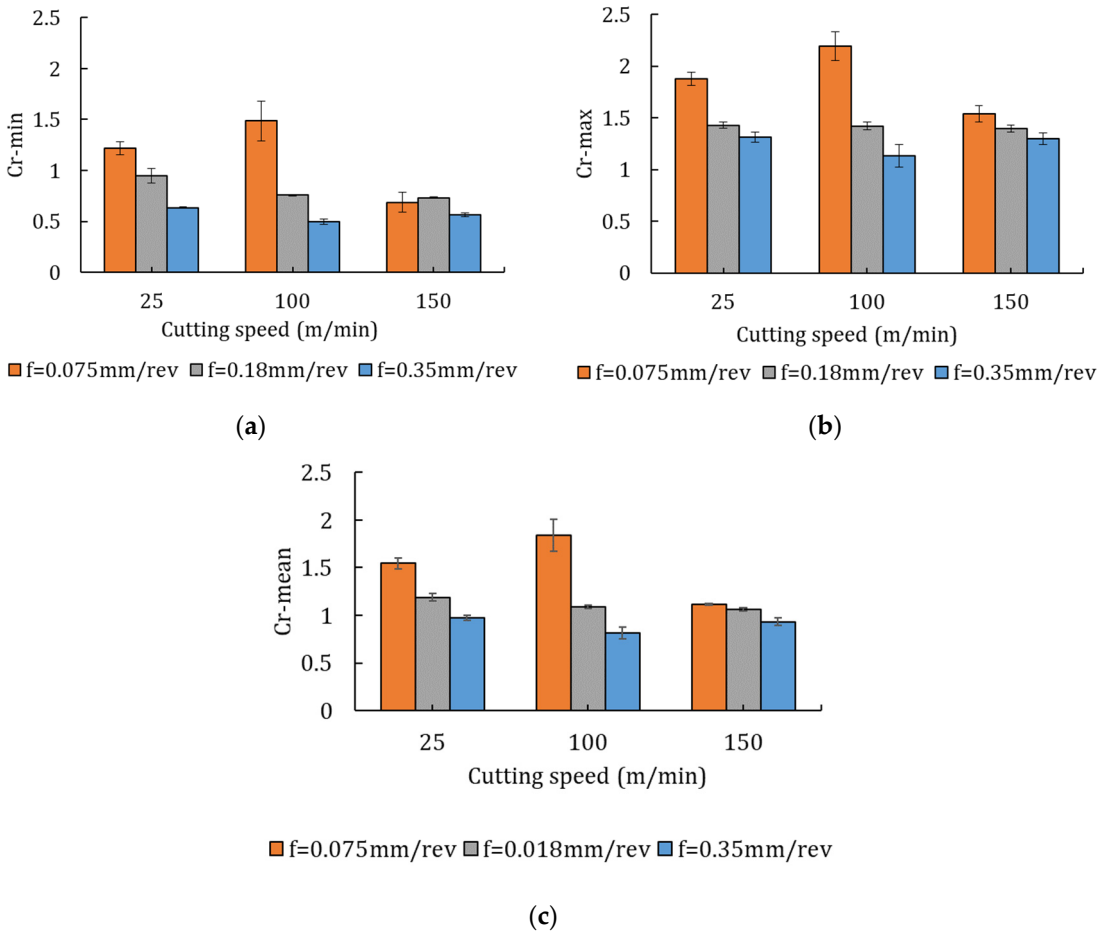


Figure 4. Evolution of compression ratios with cutting condition: (**a**) Cr-min; (**b**) Cr-max; (**c**) Cr-mean.

A decrease in the compression ratios is shown when V_c and f increase. This tendency is in good agreement with other studies on metal machining [25,26]. Astakhov [25] explains that the plastic strain reduces with V_c and f augmentation. However, the compression ratio does not provide complete information since it is more adapted to relatively continuous chips. The chip segmentation ratio is more adequate for describing the morphology of the segmented chips. For this purpose, Kouadri et al. [24] proposed a set of parameters to quantify the segmentation intensity.

In this work, the maximum segmentation ratio $SR_{\max}$ given by Equation (2) was used because its interpretation is quite clear. It varies between 0 and 1, where 0 corresponds to a continuous chip and 1 to a fragmented chip.

$$SR_{\max} = \frac{H-h}{H} \quad (2)$$

Figure 5 shows an increase in $SR_{\max}$ when the V_c and f increases, meaning that an intensification of the segmentation phenomenon occurs when there is an augmentation of material flow. This result was observed in several studies on many metals, including Ti-6Al-4V. Schulz et al. [27] named this ratio degree of segmentation and observed an increase in its value with V_c and f when machining an aluminum alloy. Joshi et al. [28] conducted

orthogonal machining experiments on Ti-6Al-4V at different environment temperatures and observed an increase in the segmentation ratio with the cutting speed for room temperature and at 260 °C.

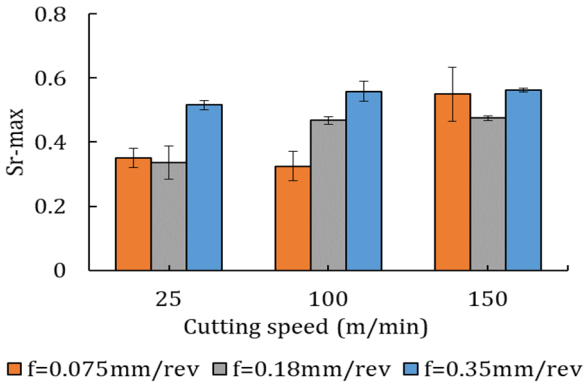


Figure 5. Segmentation ratio evolution with cutting conditions.

2.2.2. Microstructural Analysis of Chips

The initial microstructure of Ti-6Al-4V shows two phases, namely the alpha phase with a hexagonal structure and the beta phase with a cubic structure. The EBSD technique was used to estimate the proportion and distribution of these two phases and the orientation of the microstructure grains. The EBSD technique needs a high-quality surface with very low roughness to be efficient. A specimen of the un-machined material was prepared by using mechanical and semi-mechanical polishing to obtain a sub-micrometric surface roughness. Mechanical polishing hardens the polished surface and induces residual stresses, which are unfavorable to the EBSD technique. Thus, electro-polishing was used to remove the hardened layer due to the previous mechanical polishing and therefore reduced the residual stress.

Figure 6a shows a map with the alpha phase in red color while the beta phase is blue. The volume fraction of the beta phase is about 4.5%, and the grains are equiaxed with an intergranular distribution. Figure 6b presents the Inverse Pole Figure (IPF) map of the material obtained with the EBSD technique before the machining operation. There is no texture orientation since the grains seem to be randomly oriented. The initial grain size is also estimated from this map with an average of 3.13 µm for the alpha grains and 0.6 µm for beta grains. The distribution function of the grain's diameter is plotted in Figure 7 for the two phases. The other statistical values are summarized in Table 3.

Both SEM and EBSD techniques were used to analyze the microstructure in the chip, including the ASB. All observed chips were polished beforehand to sub-micrometric roughness using mechanical and semi-mechanical processes and submitted to chemical etching with a Kroll's reagent. The chemical etching was used here for two purposes: (i) revealing the grains for SEM observation and (ii) removing the hardened layer due to the mechanical polishing for the EBSD analysis. Chemical etching is not recommended when doing an EBSD analysis. However, because of the small size of chips, electro-polishing use is difficult, and therefore, chemical etching was employed to remove the hardened surface and reduce the residual stress.

The microstructure of one selected chip is shown in Figure 8, and attention was paid to the ASB and phenomena occurring in this area. Two features are especially interesting: (i) the deformation of grains by elongation, which provides key information on the ductility of the material during the shearing process leading to the chip formation and (ii) the presence and extent of cracks, which provides information on damage mechanism. In Figure 8, the ASB is constituted by a crack and localized plastic deformation area. The crack starts from the chip-free surface and propagates toward the chip surface in contact with the tool rake face. This observation is in accordance with other results, such as those obtained by Hua and Shivpuri [29]. It was noted that there was a low plastic deformation around

the cracks occurring in the ASB, meaning a lack of ductility. The gap of ductility between the inside and outside of ASB revealed a difference in the thermo-mechanical loading in the chip, namely the amount of temperature, strain rate, and hydrostatic stress.

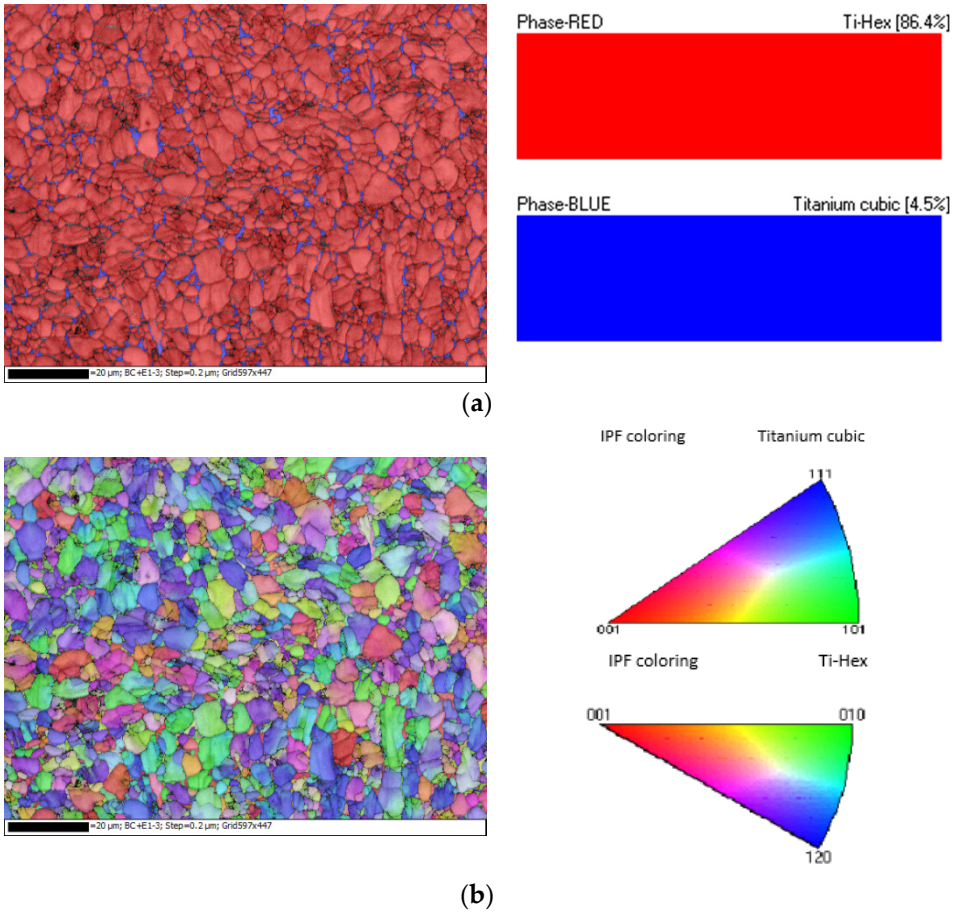


Figure 6. Initial microstructure of Ti-6Al-4V. (**a**) EBSD phase contrast map; (**b**) EBSD inverse pole figure map.

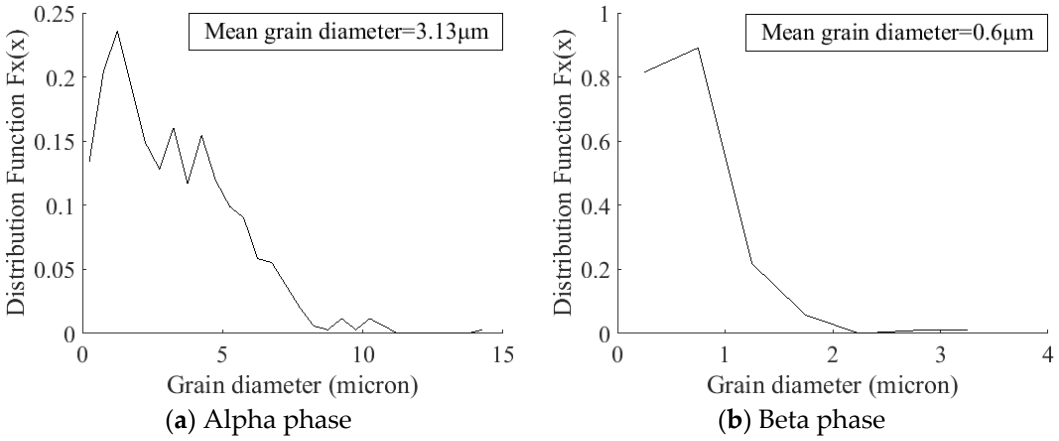


Figure 7. Initial microstructure of Ti-6Al-4V: grain diameter statistic function distribution. (**a**) Alpha phase; (**b**) Beta phase.

Table 3. Statistical values of the initial microstructure grain diameter.

	Average Value (µm)	Standard Deviation (µm)	Maximum Value (µm)	Minimum Value (µm)	Number of Indexed Grains
Alpha phase	3.13	2.2	14.2	0.2	686
Beta phase	0.6	0.4	3.1	0.2	211

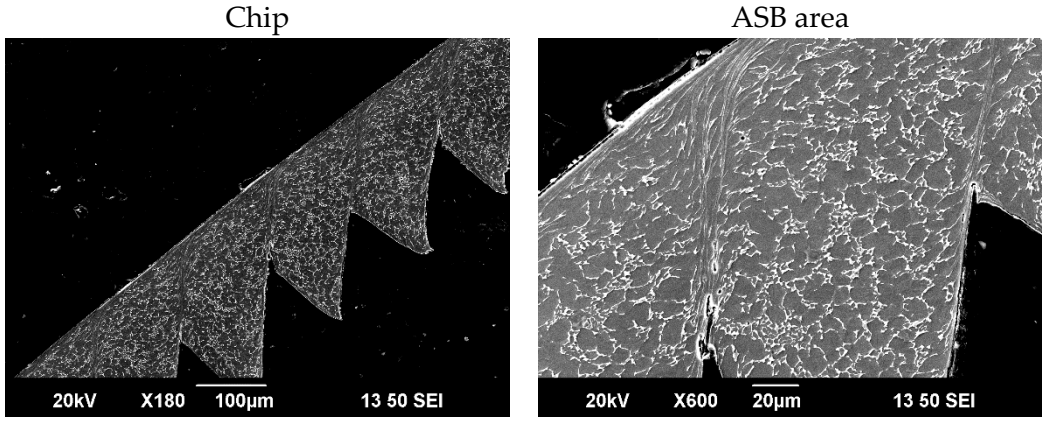
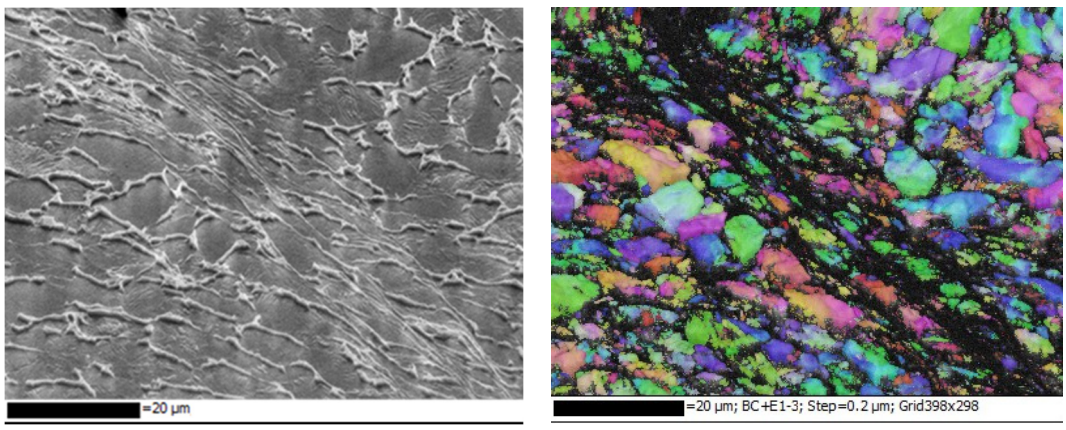


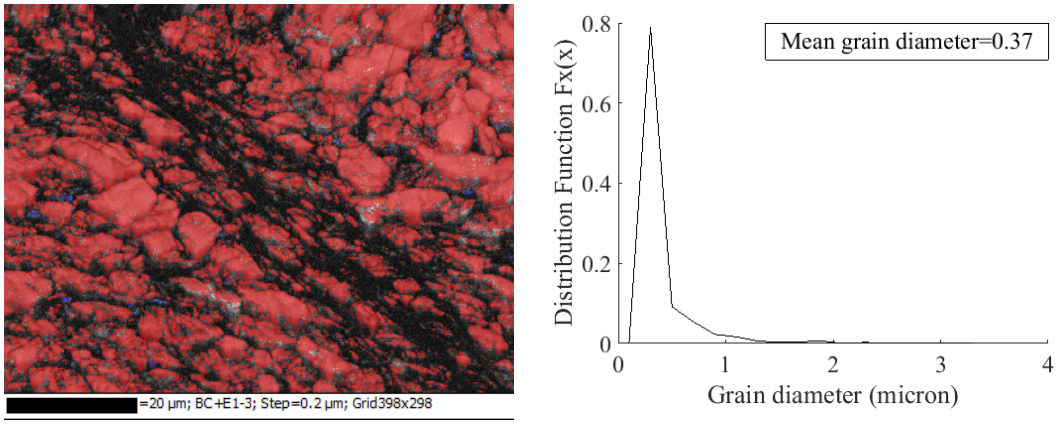
Figure 8. ASB area observed under SEM for V_c = 150 m/min and f = 0.18 mm/rev.

The ABS is analyzed using EBSD techniques to reveal if a microstructure change occurs due to the intense deformation. Figure 9a presents an ASB observed with the SEM technique, while Figure 9b presents the corresponding IPF map. This reveals a reduction in the grain size. A careful examination of Figure 9b shows that the non-indexed areas of the IPF map, appearing in black, correspond to the beta phase. This is probably due to Kroll's reagent treatment. All the other indexed grains are alpha phase grains. Figure 9c confirms this since almost all grains appear in red color, which means that it is an alpha phase. Thus, the non-indexed areas in Figure 9b are occupied by the beta grains. The distribution function of the alpha grains diameter is plotted in Figure 9d. The reduction in the grains size in the ASB is in accordance with other results, such as those of Xue et al. [14] and Wan et al. [16]. Indeed, in [14,16], grain refinement was observed in the ASB of Ti-6Al-4V chips. An average alpha grain diameter of 0.37 µm was measured in the ASB. The other statistical values are summarized in Table 4. This grain refinement is the consequence of the dynamic recrystallization phenomenon. Thus, two phenomena are responsible for the material softening: the damage mechanism and the dynamic recrystallization.



(**a**) (**b**)

Figure 9. *Cont.*



(**c**) (**d**)

Figure 9. ASB microstructure data for V_c = 100 m/min and f = 0.18 mm/rev. (**a**) SEM micrograph, (**b**) EBSD Inverse Pole Figure Map, (**c**) EBSD phase contrast map, and (**d**) distribution function of grain diameter.

Table 4. Statistic values of grains diameter in the ASB.

	Mean Value (µm)	Standard Deviation (µm)	Max. Value (µm)	Min. Value (µm)	Number of Studied Grains (µm)
Alpha phase	0.37	0.31	3.36	0.22	663

3. Multi-Physics Modelling of the Ti-6Al-4V Behavior in Machining

According to the previous experimental observations, a multi-physics behavior model for the Ti-6Al-4V alloy was developed thereafter.

3.1. Microstructure Dependent Flow Stress Model

The consideration of the microstructure evolution during machining has an important influence on material behavior. DRX causes a drop in the material flow stress because of the dislocation density decrease (Figure 10). There are several types of DRX: continuous, discontinuous, and geometric. The discontinuous dynamic recrystallization (DDRX) refers to a recrystallization process with nucleation of new grains, followed by growth. Since sub-micrometric grains are observed in this work and other references [14,16] in the ASB, DDRX was considered here. The JMAK model was thus adopted to model the microstructural transformation since it is a phenomenological model for DDRX. The strain corresponding to the onset of DDRX is called the critical strain.

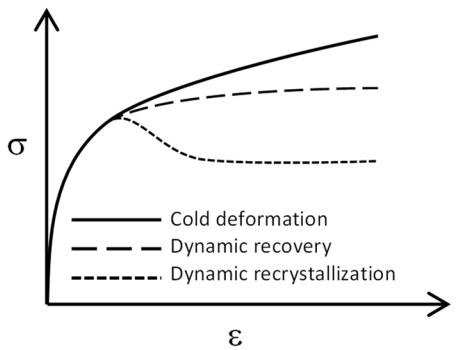


Figure 10. Illustration of dynamic recovery and recrystallization effects on flow curves.

The recrystallization critical strain ε_{crit} is predicted according to the JMAK model, given by Equation (3), where a_1, h_1, m_1, a_2 are the model parameters, Q_{act} is the activation

energy, R is the Boltzmann constant and d_0 is the initial grain size. Table 5 summarizes the adjusted values of parameters taken from [30,31] to better simulate the cutting process (see Section 4).

$$\varepsilon_{crit} = a_2 a_1 \, d_0^{h_1} \, \dot{\varepsilon}^{m1} \, \exp\left(\frac{Q_{act} m_1}{RT}\right) \tag{3}$$

Table 5. JMAK model parameters for recrystallization critical strain (adjusted based on [30,31]).

a_1	h_1	m_1	a_2	Q_{act} (kJ·mol^{-1})	R (J·K^{-1}·mol^{-1})	d_0 (µm)
0.8	0	0.01	0.4	218	8.31	3

The recrystallization of a given volume of material is not instantaneous. The first step of DDRX is new grains nucleation at the grain boundaries. Afterward, the new grains grow, replacing the old ones. The transformed proportion of the volume is called recrystallized volume fraction X_{DRX}. It is given by Equation (4) according to the JMAK model. The initial value of X_{DRX} is 0 and the maximum value is 1. Here a_5, h_5, m_5, β_d, and k_d are the model parameters. Table 6 summarizes the used adjusted values adjusted based on [30,31].

$$\begin{aligned} &X_{DRX} = 1 - \exp\left[-\beta_d \left(\tfrac{\varepsilon - \varepsilon_{crit}}{\varepsilon_{0.5}}\right)^{k_d}\right] \text{ if } \varepsilon \geq \varepsilon_{crit} \\ &\dot{X}_{DRX} = 0 \text{ if } \varepsilon < \varepsilon_{crit} \\ &\text{with } \varepsilon_{0.5} = a_5 \, \dot{\varepsilon}^{m5} \, \exp\left(\tfrac{Q_{act} m_5}{RT}\right) \end{aligned} \tag{4}$$

Table 6. JMAK model parameters for DDRX kinetics (adjusted based on [30,31]).

a_5	h_5	m_5	β_d	k_d
0.022	0	0.03	2	2

As shown in Figure 9, some areas in the chips are severely deformed and transformed when other zones are undeformed or slightly deformed. In the slightly deformed areas, the material does not undergo a microstructural transformation and is only affected by hardening, strain rate, and thermal softening. The severely deformed material is also affected by the microstructure transformation softening by the mechanism of DDRX. Therefore, the flow stress, noted σ_{Hybrid}, was suggested similar to a sum of two different flow stresses weighted by their respective volume fraction of DRX (X_{DRX}). This hybrid flow stress was calculated according to the Equation (5). In this paper, the untransformed material flow stress σ_1 was calculated according to the JC model, given by Equation (6). The transformed material flow stress σ_2 was calculated according to the TANH flow stress model, given by Equation (7). The model parameters were taken from [18,22] and listed in Table 7.

$$\sigma_{Hybrid} = (1 - X_{DRX})\sigma_1 + X_{DRX}\sigma_2 \tag{5}$$

where

$$\begin{aligned} &\sigma_1 = \sigma_2 = f_\varepsilon \cdot f_{\dot{\varepsilon}} \cdot f_T \\ &f_\varepsilon = A + B\varepsilon^n \\ &f_{\dot{\varepsilon}} = 1 + C \ln\left(\tfrac{\dot{\varepsilon}}{\dot{\varepsilon}_0}\right) \\ &f_T = 1 - \left(\tfrac{T - T_0}{T_m - T_0}\right)^m \end{aligned} \tag{6}$$

and

$$\begin{aligned}
\sigma_2 &= f_\varepsilon \cdot f_{\dot{\varepsilon}} \cdot f_T \cdot f_{\varepsilon,T} \\
f_\varepsilon &= A + B\varepsilon^n (\exp(\varepsilon^a))^{-1} \\
f_{\dot{\varepsilon}} &= 1 + C \ln\left(\frac{\dot{\varepsilon}}{\dot{\varepsilon}_0}\right) \\
f_T &= 1 - \left(\frac{T - T_0}{T_m - T_0}\right)^m \\
f_{\varepsilon,T} &= f_{\varepsilon,T} = 1 - \left(\frac{T}{T_m}\right)^d \left[1 + \tanh\left(\left(\varepsilon + \left(\frac{T}{T_m}\right)^b\right)^{-c}\right)\right]
\end{aligned} \tag{7}$$

Table 7. JC and TANH models parameters [18,22].

A (MPa)	B (MPa)	C	m	n	T_0 (K°)	$\dot{\varepsilon}_0$ (s^{-1})	a	b	c	d
968	380	0.02	0.577	0.421	298	1	1.6	0.4	6	0.5

3.2. Microstructure Dependent Damage Model

Different micrographs show that ductile fracture appears during the chip formation. The fracture strain ε_f is predicted according to the Johnson–Cook damage (JCD) model (see Equation (8)), where $d_1 - d_5$ are parameters taken from [32,33] (see Table 8).

$$\varepsilon_f = \left[d_1 + d_2 \exp\left(d_3 \frac{P}{\sigma_y}\right)\right]\left[1 + d_4 \ln\left(\frac{\dot{\varepsilon}}{\dot{\varepsilon}_0}\right)\right]\left[1 + d_5 \frac{T - T_0}{T_m - T_0}\right] \tag{8}$$

Table 8. JCD model parameters [32,33].

d_1	d_2	d_3	d_4	d_5
−0.09	0.25	−0.5	0.014	3.87

Since the strain rate and the temperature change when the material is deformed, the fracture strain value changes with the thermo-mechanical conditions. Therefore, the damage initiation parameter w is used to quantify the amount of plastic deformation necessary to initiate the material failure. Its initial value is 0, and when w reaches 1, the material properties start to undergo degradation. It is calculated according to Equation (9).

$$w = \int \frac{d\varepsilon}{\varepsilon_f} \tag{9}$$

The plastic strain corresponding to the degradation initiation is ε_0. Once the material properties degradation starts, micro-voids and cracks nucleate and grow. There is a coalescence of these defects leading to complete degradation of the material and then to its fracture. Hillerborg's criterion (Equation (10)) was used to calculate the deformation energy necessary for fracture occurrence.

$$G_f = \int_{u_0}^{u_f} \sigma_y du \tag{10}$$

where G_f is the fracture energy, u_0 and u_f are the plastic displacement at the initiation of material degradation and the plastic displacement at fracture, respectively.

The damage variable d quantifies the damage accumulation. It varies from 0 (no damage) to 1 (fully damage) and affects the flow stress σ_y as follows:

$$\sigma_y = (1 - d)\sigma_{Hybrid} \tag{11}$$

Recrystallization is a restoration process that allows the material to recover its properties. This means that the material undergoes healing, and the damage is reduced as its ductility increases. Several damage models taking into account healing due to recrystallization can be found in the literature (e.g., [34,35]). Shang et al. [21] studied the influence of DRX on material damage. They observed that DRX impedes damage evolution by stopping void and hinders defects coalescence. They explained that DRX occurrence tends to relax stress concentration and thus prevents damage. Based on this analysis, it is postulated that DRX prevents damage occurrence. Therefore it is assumed that the material can either undergo recrystallization or damage, but not the two phenomena at the same time and in the same location.

Based on this analysis, a damage evolution model considering the DRX occurrence was proposed, given by Equation (12). Until the degradation occurs, d is equal to 0. Once the degradation starts ($\varepsilon = \varepsilon_0$), the damage variable d increases until it reaches 1. Thus, the flow stress becomes 0 and the fracture occurs.

$$\dot{d} = \begin{cases} \frac{L\dot{\varepsilon}}{u_f} & \text{if } (\varepsilon < \varepsilon_{crit} \text{ and } w = 1) \\ 0 & \text{if } (\varepsilon \geq \varepsilon_{crit} \text{ or } w < 1) \end{cases} \tag{12}$$

3.3. Application of the Coupled Microstructure-Damage Model

The proposed multi-physics behavior model is applied firstly for a uniaxial tension loading in isothermal and fixed stain rate conditions to understand the stress-strain response of the model and associated variables (DRX and damage). Therefore, various temperature/strain rate couples are considered hereafter.

Figure 11a illustrates how the temperature affects the material flow stress for strain rate set to 10^3 s^{-1}. Three temperatures are chosen (25, 500, and 800 °C). At a room temperature of 25 °C, the material undergoes low plastic strain up to fracture. For higher temperatures, the material undergoes dynamic recrystallization and high deformation. Figure 11c shows the corresponding recrystallized volume fraction X_{DRX} evolution with temperature. For a low temperature (25 °C), the critical strain is elevated. The rate of recrystallization is also lower compared to the other cases. With an increase in the temperature (here 500 °C and 800 °C), the critical strain decreases, and the recrystallization rate is higher. Since DRX is a thermally activated phenomenon, this evolution was expected. Figure 11e shows the associated damage evolution. The plastic deformation at damage initiation increases with temperature. At higher temperatures (800 °C), the damage does not occur since recrystallization occurs first, which deactivates the damage.

Figure 11b shows how strain rate affects the material flow stress for temperature set to 500 °C. Three strain rates are chosen (1, 10^3, 10^5 s^{-1}). At a low strain rate (1 s^{-1}), recrystallization and high deformation occur. For higher strain rates, fractures are observed. Figure 11d shows the dependency of recrystallized volume fraction X_{DRX} on strain rate. It is observed that an increase in strain rate delays the occurrence of DRX. Figure 11f shows that for higher strain rates, damage occurs first, which in turn deactivates the DRX. No damage occurrence is observed for the lower strain rate of 1 s^{-1} and a temperature of 500 °C.

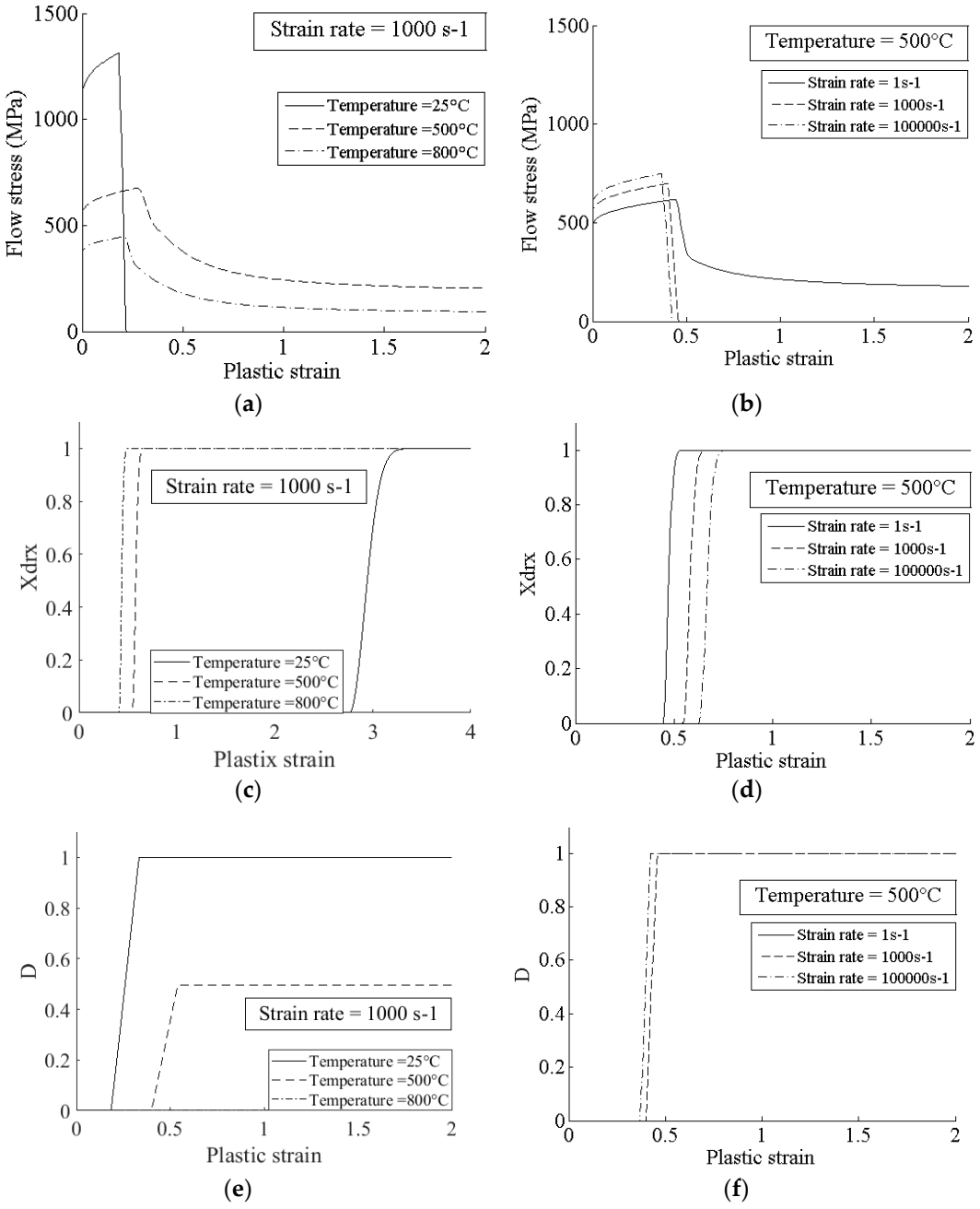


Figure 11. Temperature and strain-rate effects on the (**a**,**b**) flow stress, (**c**,**d**) recrystallized volume fraction, and (**e**,**f**) damage.

3.4. Grain Size Evolution

The recrystallized grain size d_{DRX} can be predicted thanks to the JMAK model. Equation (13) gives the expression of the grain size evolution. a_8, n_8, and m_8 are the model parameters. d_0 is the initial grain size of the material, namely the as-received material microstructure. This initial grain size is chosen considering the average grain size of the measured alpha grains (3.13 µm), as reported in Table 3. Table 9 summarizes the parameters used in Equation (13), adjusted based on [30]. The average grain size is calculated with Equation (14).

$$d_{DRX} = a_8 \varepsilon^{n8} \dot{\varepsilon}^{m8} \exp\left(\frac{Q_{act} m_8}{RT}\right) \tag{13}$$

$$d_{avg} = X_{DRX} d_{DRX} + (1 - X_{DRX}) d_0 \tag{14}$$

Table 9. JMAK model parameters for grain size prediction (adjusted based on [30]).

a_8	n_8	m_8	d_0 (μm)
3	0	−0.03	3

4. Application for Machining Simulations

The proposed multi-physics behavior model, coupling microstructure and damage evolutions were adopted for the simulation of the chip formation process when machining Ti-6Al-4V alloy.

A 2D Lagrangian FE approach was adopted, in the Abaqus/explicit code, to simulate the performed orthogonal cutting tests. The workpiece was divided into three parts: chip of f initial thickness, separation layer of 30 μm, and machined part (see Figure 12). The tool and workpiece were meshed with a coupled temperature–displacement plane strain FE of type CPE4RT (4-node bilinear displacement and temperature, with reduced integration and hourglass control). The mesh is refined in the chip and separation layer, with a mesh size of 10 μm. A progressive mesh was applied in the workpiece, with the minimum size of 10 × 10 μm in the chip and the maximum size of 50 × 10 μm at the limits where boundary conditions are applied. A progressive mesh was also applied to the tool with a mesh size of the same order as in the chip (10 μm) to capture well the tool–work material contact.

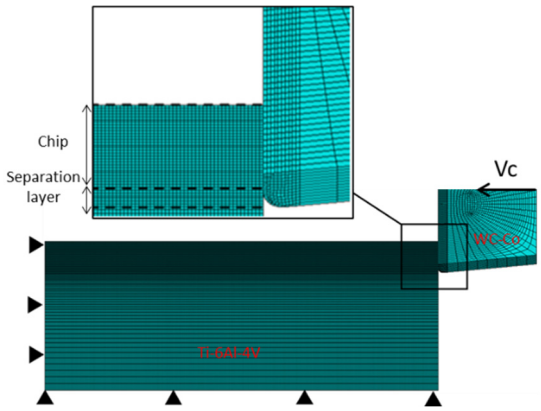


Figure 12. Two-dimensional Lagrangian finite element model for the orthogonal cutting simulation.

The constitutive equations described before were implemented using the user material subroutine (VUMAT) of Abaqus/explicit code to capture the behavior of the work material Ti-6Al-4V. The tool was modeled as a rigid body for which the cutting speed V_c is applied. The basic thermomechanical properties of the workpiece and tool materials are reported in Table 10.

Table 10. Mechanical properties of workpiece and tool materials [22].

	E (GPa)	λ (W/mK)	α (K^{-1})	C_P (J/kgK)	ρ (kg/m^3)
Ti-6Al-4V	113.8	7.3	8.6×10^{-6}	580	4430
WC–Co	800	46	4.7×10^{-6}	203	15,000

Since the problem involves interaction between the tool and work material, in the FE model, the mechanical contact condition was modeled by the Coulomb friction without limitation. The coefficient of friction (COF) was adjusted to 0.6 (according to the ratio of measured cutting forces and well capturing the cutting process), and the sliding stress was not limited by the shear yield stress. The thermal contact condition was considered by the frictional heat at the tool–work material interface assumed to diffuse totally (η_f = 1) and

equally in the work material and tool, so the heat partition coefficient β was set to 0.5. A high value of the heat transfer coefficient h_t was introduced to the interface temperature from either side of the contact. All equations of the friction model and the heat balance at the tool–work material interface are given by Equation (15) and can be found in [36]. The thermomechanical contact parameters are reported in Table 11.

$$\begin{aligned} \tau_f &= \min(\mu\,\sigma_n, \tau_{\lim}) \\ \dot{q}_f &= \mu\,\sigma_n v_s \\ \dot{q}_t &= \beta\,\eta_f \dot{q}_f + h\,(T_w - T_t) \\ \dot{q}_w &= (1-\beta)\,\eta_f \dot{q}_f - h\,(T_w - T_t) \end{aligned} \tag{15}$$

Table 11. Tool–work material interface parameters.

COF	$\tau_{\lim}$ (MPa)	η_f	β	h_t (mW/mm^2 °C)
0.6	no limit	1	0.5	2000

4.1. Chip Morphology

The predicted chips morphology was analyzed and compared to the experimental measurements. Figure 13 shows a segmented chip with crack formation for the case of V_c = 100 m/min and f = 0.18 mm/rev. The partial fracture of the chip was reproduced by the simulation with a crack initiation in the ASB from the chip-free surface, as in Figure 13c. The chip morphology parameters are measured and compared to the experimental ones for each case. Three chip segments are measured; average and deviation values are reported.

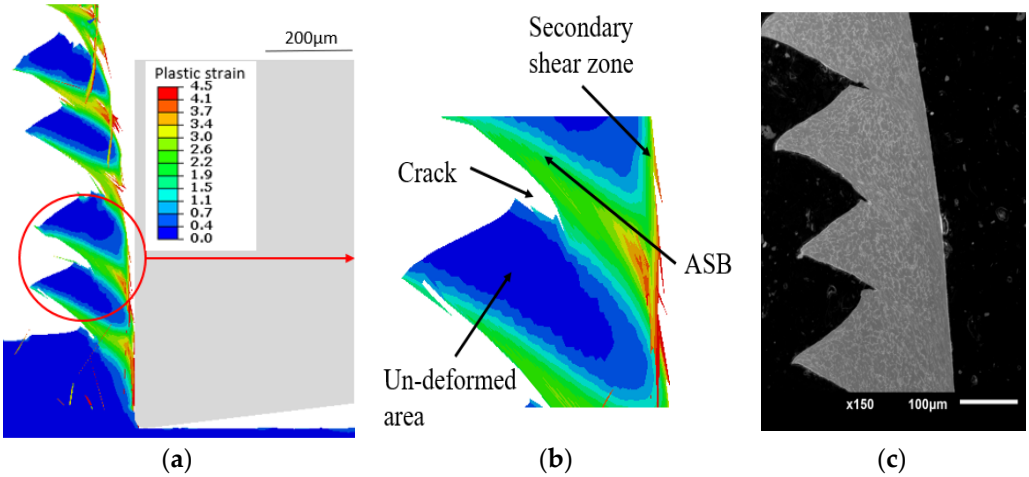


Figure 13. Chip morphology for V_c = 100 m/min and f = 0.18 mm/rev: (**a**) simulated chip, (**b**) segment details, and (**c**) characterized chip.

Figure 14 shows the experimental and numerical chips for a low feed (0.075 mm/rev). The aperiodic chip segmentation is well reproduced. The higher cutting speed leads to the intensification of segmentation. Figure 15 shows the corresponding chip morphology parameters. For V_c = 25 and 100 m/min, the difference between the experimental and the numerical results is not negligible; this is attributed to the instability of segmentation for these conditions (aperiodic chip segmentation). The intensification of segmentation for V_c = 150 m/min is reproduced by the simulation, and the other chip morphology parameters are well predicted for this case.

Figure 16 shows the case of f = 0.18 mm/rev. The chip segmentation is more pronounced in comparison to the case of f = 0.075 mm/rev. This result confirms the effect of feed on the chip segmentation. The simulated chip, corresponding to f = 0.18 mm/rev

and V_c = 100 m/min, is quasi-periodic. This corroborates the experimental results. The segmented chip presents cracks in the ASB when it is almost inexistent for the case of low feed (0.075 mm/rev).

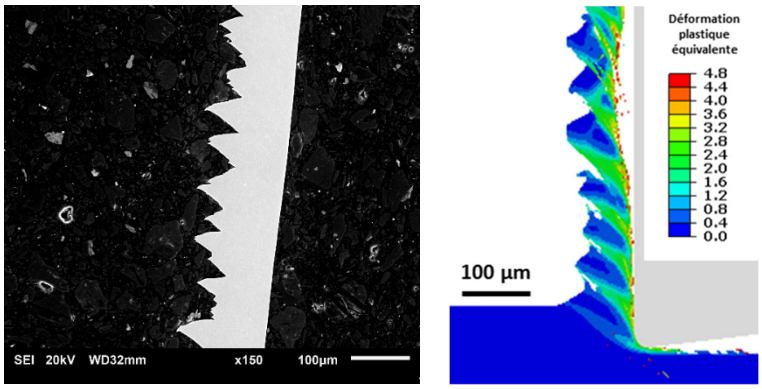


Figure 14. Experimental vs. simulated chip for V_c = 100 m/min and f = 0.075 mm/rev.

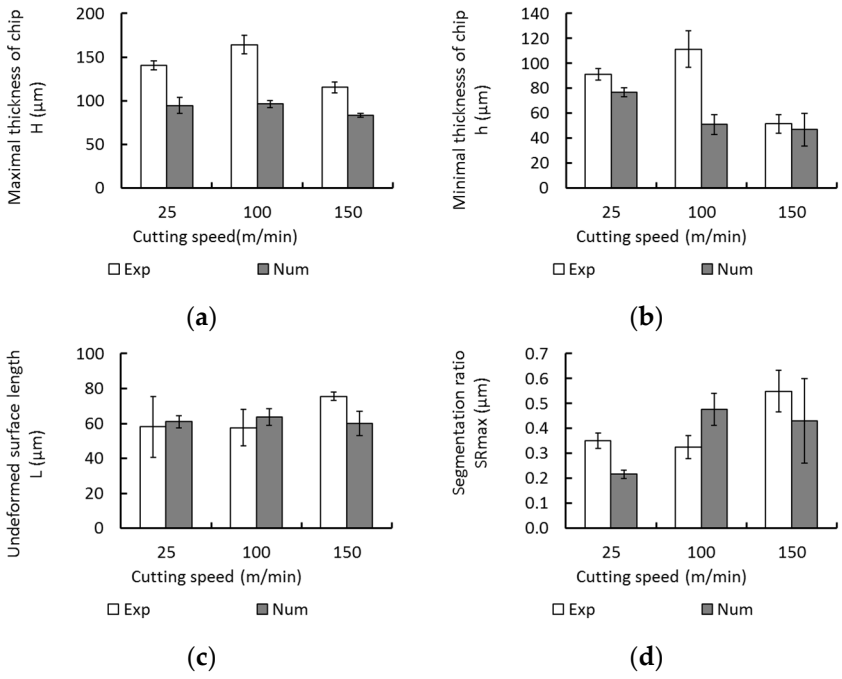


Figure 15. Comparison of chip morphology parameters for f = 0.075 mm/rev.

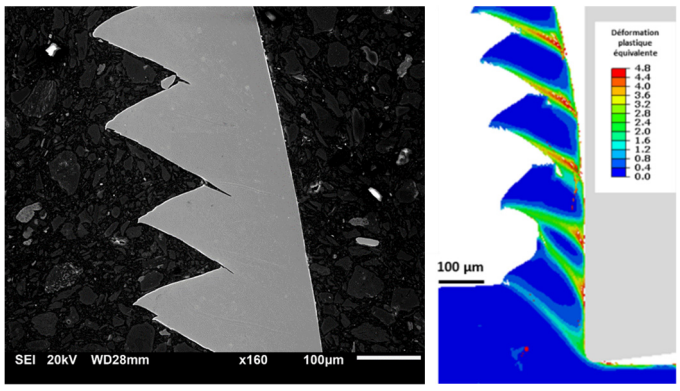


Figure 16. Experimental vs. simulated chip for V_c = 100 m/min and f = 0.18 mm/rev.

Figure 17 shows the corresponding chip morphology parameters. According to the simulations, the deformed thicknesses, H and h, decrease with cutting speed rise, while the deformed surface length L increases. Segmentation ratio SR_{max} increases when V_c raises from 25 m/min to 100 m/min and remains constant when V_c = 150 m/min. These observed trends are in good accordance with the experimental result, except for the decrease in H observed for the numerical chips, while it does not seem to vary experimentally.

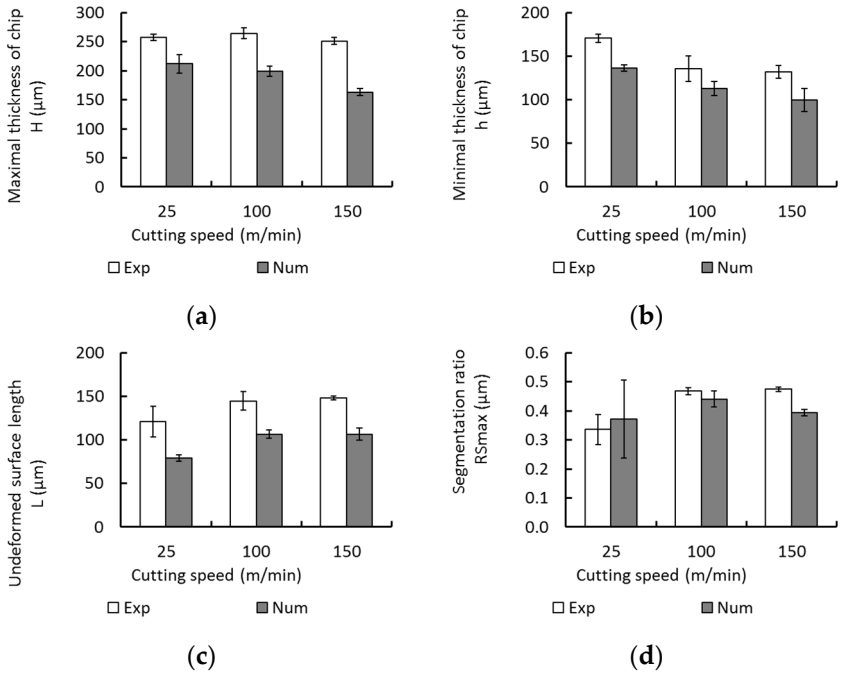


Figure 17. Comparison of chip morphology parameters for f = 0.18 mm/rev.

Various sources can explain gaps between experimental and predicted geometric parameters, shown in Figures 15 and 17. The major one is that the parameters of the proposed behavior model of Ti-6Al-4V were taken from the literature and may not correspond finely to the machined Ti-6Al-4V alloy here. The complex contact at the tool–work material interface may be miscaptured by the adopted friction thermomechanical model, which highly affects the chip flow. Moreover, the chip formation by FE deletion at the separation layer alters the formation process of the ASB, giving rise to the chip thickness variation. Indeed, premature damage initiation in the separation layer leads to low chip segmentation; on the other hand, delayed damage leads to intense chip segmentation. Rigorously, pertinent damage criterion (formulation and identified parameters) improves the prediction quality. Finally, the FE method is well known as nonobjective (mesh size and FE type dependency) and affects the prediction quality, particularly when simulating complex forming processes (involving large deformation), such as machining.

4.2. Microstructure Evolution in the Chip

4.2.1. Grain Size Evolution

The grain size in the machined part is an indicator of the microstructure evolution. Figure 18 presents the areas in the chip and at the machined surface which undergo DRX. The transformed regions are where the plastic strain is important, meaning the ASB, the secondary shear zone, and the machined surface. The recrystallized grain size is estimated with the JMAK Equation (13). The average grain size is therefore calculated using Equation (14).

The recrystallized grain size is smaller than the initial one. An observation of the recrystallized areas in the chip (see Figure 19c) shows that the grains located in the middle of the ASB are a larger size than at the tool–chip interface and at the free surface. The JMAK

model is an Arrhenius equation, and therefore, grain size increases with temperature and decreases with strain rate. Knowing that the temperature and strain rate decrease from the tool–chip interface to the free surface (Figure 19a,b), the grains at the interface are bigger because of the higher temperature, and the grains at the free surface are bigger because of the lower strain rate.

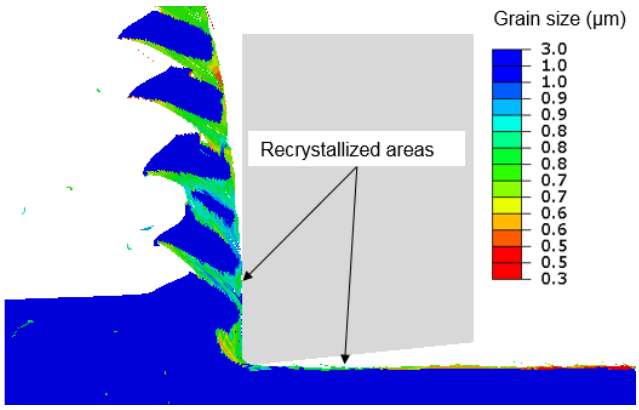


Figure 18. Grain size distribution for V_c = 100 m/min and f = 0.18 mm/rev.

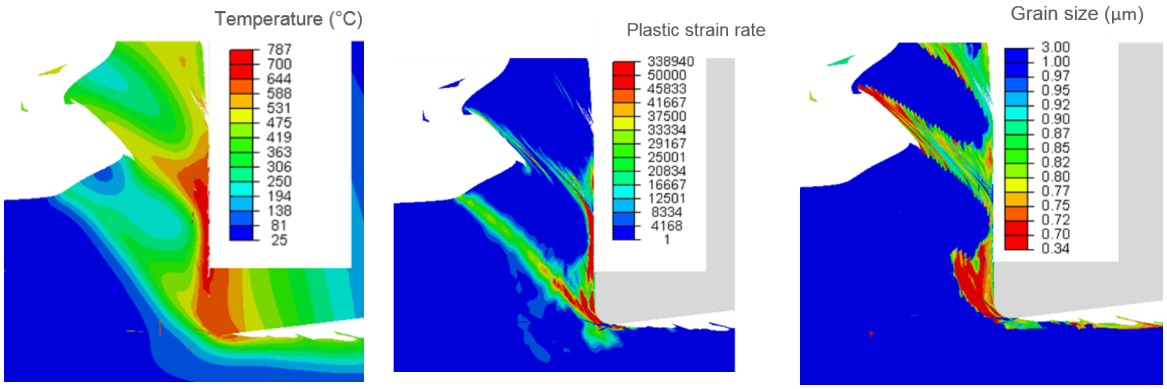


Figure 19. Simulated fields for V_c = 100 m/min and f = 0.18 mm/rev: (**a**) temperature, (**b**) strain rate, and (**c**) grain size.

Three locations in the ASB are chosen to analyze the effect of cutting conditions on the grain size evolution: one near the tool–chip interface, one taken in the middle of the ASB, and the last one is close to the chip-free surface, as shown in Figure 20.

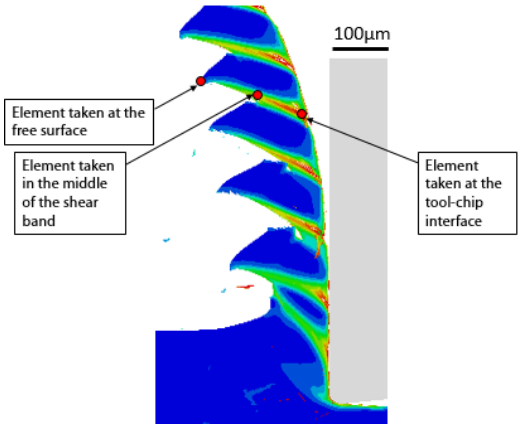


Figure 20. Location of selected elements in the shear band for grain size analysis.

Figure 21 shows the estimated grain size in the different locations in the chip indicated in Figure 20 for all cutting conditions. There is no notable tendency concerning the effect of the feed. In contrast, the cutting speed seems to increase the recrystallized grain size, which can be explained by the effect of the heating rise as the cutting speed increases.

Figure 22a shows the simulated grain size at the generated surface. Except for the case of V_c = 25 m/min and f = 0.18 mm/rev, the trend is the same as in the chip, meaning no tendency for the feed and an increase in grain size with cutting speed. Figure 22b shows the thickness of the surface layer affected by recrystallization, which varies between 5 and 30 µm. When cutting speed or feed increases, there is an augmentation of the plastic strain, and so the temperature rises due to heat generation by plastic deformation. These modifications extend the recrystallization phenomenon and explain why the affected thickness increases with V_c and f.

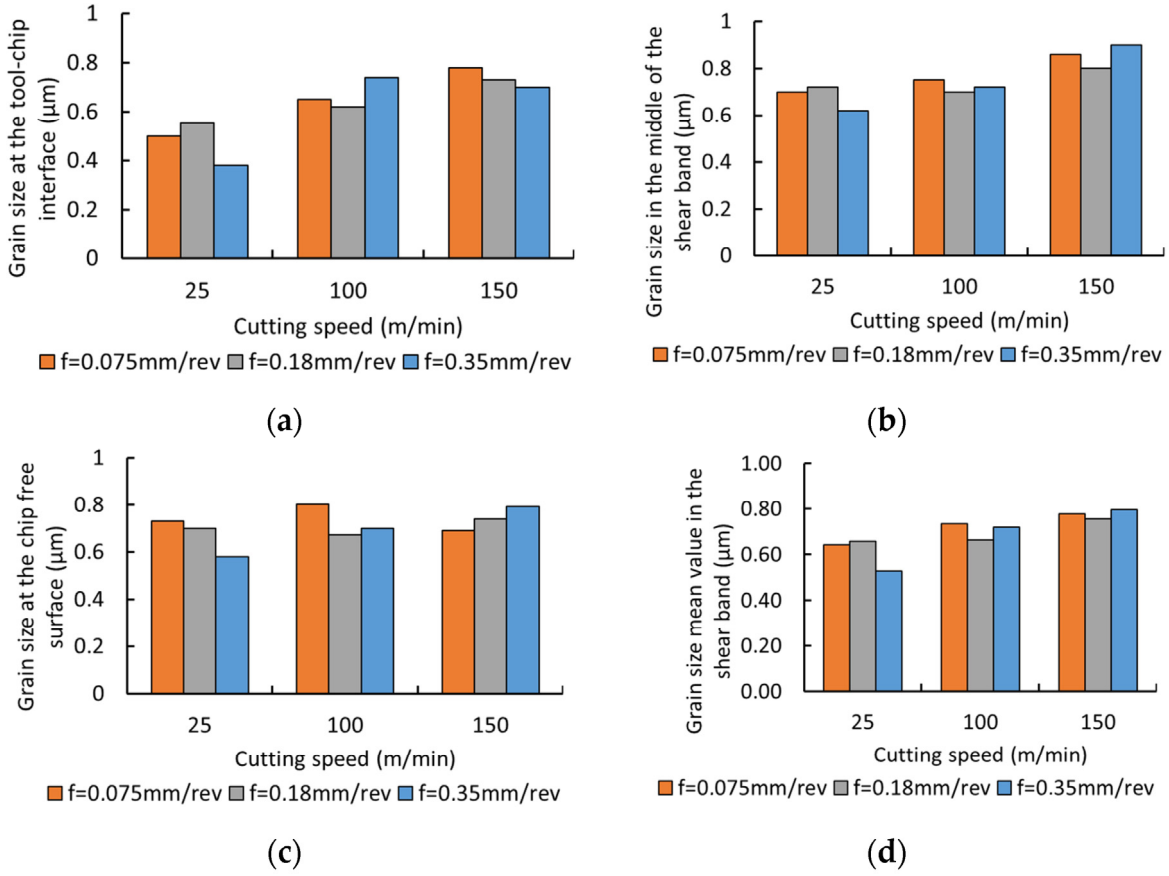


Figure 21. Grain size in the ASB estimated by simulations at (**a**) tool–chip interface, (**b**) middle of the ASB, (**c**) chip-free surface, and (**d**) mean value.

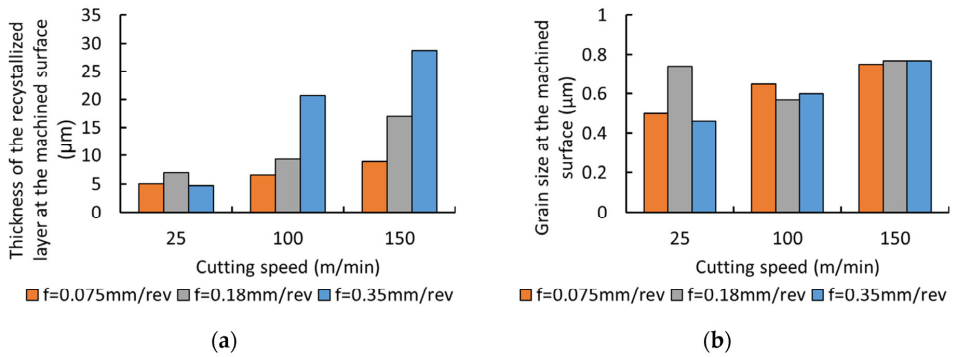


Figure 22. Simulated (**a**) thickness of the recrystallized layer and (**b**) grain size at the machined surface.

4.2.2. Link with Chip Segmentation

The link between the chip segmentation process and cutting force oscillation was established experimentally by Komanduri and Brown [37] and using FE simulation by Atlati et al. [23]. Here the mechanism of chip segmentation is related to the microstructure and damage evolution in the primary shear zone. A chip segment is limited by two successive ASB. After a complete formation of the first ASB, the development of the second ASB leads to the formation of one segment. Figure 23 shows the mechanism of a chip segment formation by the development of the ASB in the primary shear zone. A storyline in three steps is then proposed: (i) the first step corresponds to the initiation of the shear band at the tool tip, where a concentration of deformation appears accompanied by damage. The damage process starts at the tool tip and is quickly stopped by the recrystallization initiation. The recrystallization is accompanied by grain size reduction. (ii) In the second phase, the localized deformation is intensified and extended to the chip-free surface, meaning the propagation of the shear band toward the chip-free surface. Although the damage increases faster near the tool tip, fracture initiation happens at the free surface. At the same time, recrystallization occurs in the shear band with initiation at the tool tip. Since recrystallization prevents the damage process, the fracture initiation occurs preferentially where the DRX phenomenon is the weakest, meaning the free surface. (ii) Phase three is the continuation of the phenomena of the previous step, leading to the formation of the segment, which slides on the tool, and a new segment starts to form. Correspondence can be established between the cutting force and the different phases identified previously. The first phase is the initiation of the ASB and corresponds to a low value of the cutting force. The second phase is accompanied by a raise of the cutting force and finishes when it reaches the maximal value. The third phase corresponds with the end of the formation of the segment and ends when the cutting force is once again at the minimal value.

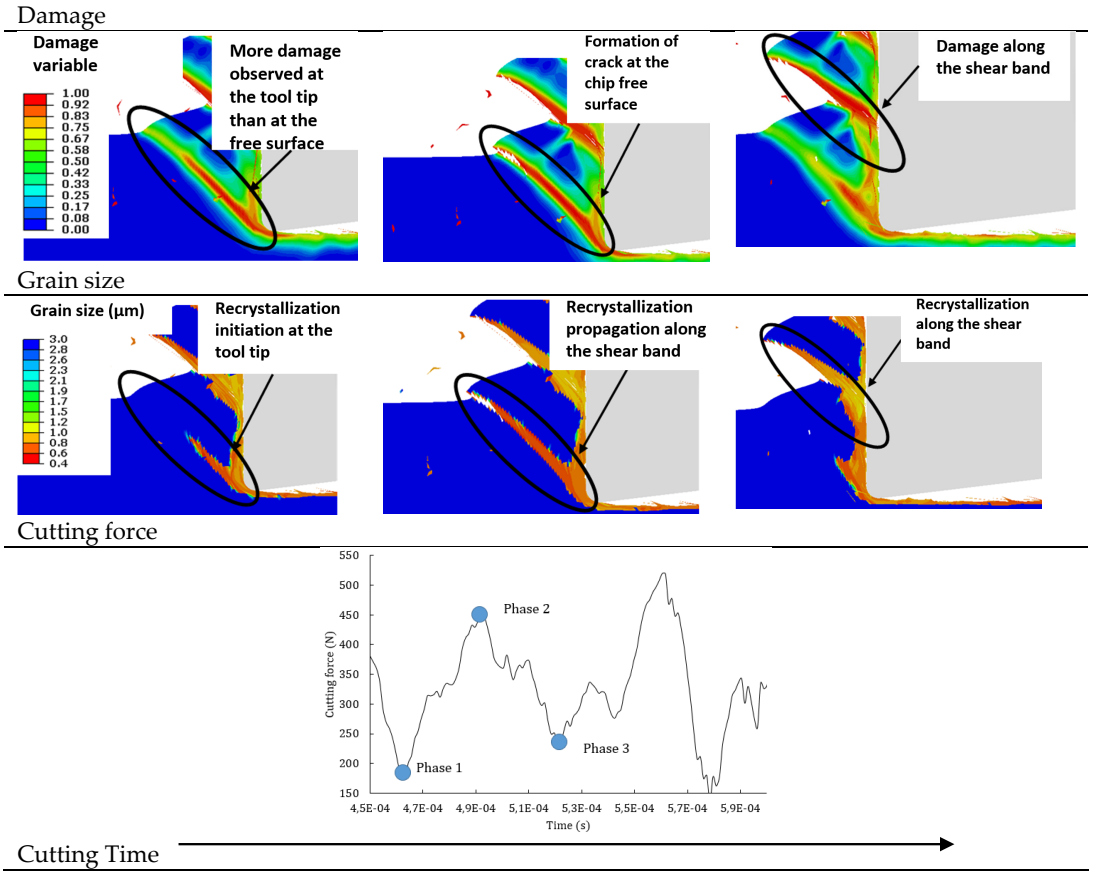


Figure 23. Link between microstructure/damage evolutions and chip segmentation process.

5. Conclusions

The material behavior of Ti-6Al-4V alloy in dry machining is investigated, with a focus on the mechanism of chip formation and the link between microstructure change and damage occurrence.

1. The characterization of chips morphology shows a classical result for refractory alloys, such as Ti-6Al-4V: increasing feed and cutting speed intensify chip segmentation;
2. The microstructure analysis of the ASB revealed the grains refinement and its interaction with damage;
3. The proposed physical behavior model of Ti-6Al-4V considers this interaction. The simulated uniaxial tension showed how combined temperature/strain rate affects damage and DRX and, in turn, the stress/strain response (flow stress);
4. The application of the material behavior model for FE simulation of machining Ti-6Al-4V showed the transition between unstable (aperiodic) and stable chip segmentation (periodic);
5. In the ASB, giving rise to the chip segmentation, the DRX and damage were predicted, with fracture occurring from the chip-free surface propagating along with the ASB, while the DRX occurs in the ASB from the tool–chip interface;
6. Finally, the material behavior model, implemented for FE simulation of machining, gives more insight into the mechanism of chip formation, particularly the interaction between DRX and damage. However, including a FE re-meshing of the cutting zone allows better results by correctly capturing the action at the tool tip and therefore what happens at the generated surface.

Author Contributions: Conceptualization: B.H., M.N. and D.Y.; Methodology: B.H. and M.N.; Experiments: D.Y. and H.M.; Software: D.Y. and B.H.; Supervision: B.H., M.N. and H.M.; Writing—original draft preparation, B.H., D.Y. and M.N.; Writing—review and editing: B.H. All authors have read and agreed to the published version of the manuscript.

Funding: This research received no external funding.

Institutional Review Board Statement: Not applicable.

Informed Consent Statement: Not applicable.

Data Availability Statement: Not applicable.

Conflicts of Interest: The authors declare no conflict of interest.

Nomenclature

Basic parameters

E	Young modulus
ρ	Material density
α	Thermal expansion
λ	Thermal conductivity
C_p	Specific Heat

Variables

ε	Equivalent plastic strain
$\dot{\varepsilon}$	Equivalent plastic strain rate
T	Temperature
σ	von Mises stress
d	damage variable

JC parameters	
A	Initial yield stress
B	Hardening modulus
C	Strain rate dependency
m	Thermal softening
n	Strain hardening
T_0	Reference Temperature
T_m	Melting Temperature
Damage parameters	
d_1, d_2, d_3, d_4, d_5	Johnson–Cook damage initiation
w	Damage initiation criteria
G_f	Fracture energy
u_0	Plastic displacement at damage initiation
u_f	Plastic displacement at fracture
JMAK model parameters	
X_{DRX}	Recrystallized volume fraction
Q_{act}	Dynamic recrystallization activation energy
R	Boltzmann constant
ε_{crit}	Critical equivalent plastic strain
$a_1, h_1, m_1, a_2,$	Critical strain
$a_5, h_5, m_5, \beta_d,$	Recrystallized volume fraction
$a_8, n_8, m_8, d_0,$	Grain size
TANH model parameters	
a, b, c, d	TANH model
Contact/friction parameters	
τ_f	Sliding stress
σ_n	Normal stress
μ	Coefficient of friction
v_s	Sliding velocity
h	Heat transfer coefficient
β	Heat partition coefficient
η_f	Friction heat ratio
$\dot{q}_f$	Friction heat
$\dot{q}_t$	Friction heat to the tool
$\dot{q}_w$	Friction heat to the work material
T_w	Interface work material temperature
T_t	Interface tool temperature
Cutting parameters	
V_c, f	Cutting speed and feed
Chip geometrical parameters	
H, h	Max. and min. chip thickness
L	Chip surface length
l_S	Chip segments peak to peak distance
CR	Chip compression ratio
SR_{Max}	Segmentation ratio maximal value

References

1. Sun, S.; Brandt, M.; Dargusch, M.S. Characteristics of Cutting Forces and Chip Formation in Machining of Titanium Alloys. *Int. J. Mach. Tools Manuf.* **2009**, *49*, 561–568. [CrossRef]
2. Ginting, A.; Nouari, M. Surface Integrity of Dry Machined Titanium Alloys. *Int. J. Mach. Tools Manuf.* **2009**, *49*, 325–332. [CrossRef]
3. Ulutan, D.; Ozel, T. Machining Induced Surface Integrity in Titanium and Nickel Alloys: A Review. *Int. J. Mach. Tools Manuf.* **2011**, *51*, 250–280. [CrossRef]
4. Donachie, M.J. *Titanium: A Technical Guide*; ASM International: Materials Park, OH, USA, 2000; ISBN 0-87170-686-5.
5. Su, G.; Liu, Z.; Li, L.; Wang, B. Influences of Chip Serration on Micro-Topography of Machined Surface in High-Speed Cutting. *Int. J. Mach. Tools Manuf.* **2015**, *89*, 202–207. [CrossRef]
6. Nakayama, K.; Arai, M.; Kanda, T. Machining Characteristics of Hard Materials. *CIRP Ann.-Manuf. Technol.* **1988**, *37*, 89–92. [CrossRef]

7. Umbrello, D. Finite Element Simulation of Conventional and High Speed Machining of Ti6Al4V Alloy. *J. Mater. Process. Technol.* **2008**, *196*, 79–87. [CrossRef]
8. Aurich, J.C.; Bil, H. 3D Finite Element Modelling of Segmented Chip Formation. *CIRP Ann. Manuf. Technol.* **2006**, *55*, 47–50. [CrossRef]
9. Cheng, W.; Outeiro, J.; Costes, J.-P.; M'Saoubi, R.; Karaouni, H.; Astakhov, V. A Constitutive Model for Ti6Al4V Considering the State of Stress and Strain Rate Effects. *Mech. Mater.* **2019**, *137*, 103103. [CrossRef]
10. Xu, X.; Outeiro, J.; Zhang, J.; Xu, B.; Zhao, W.; Astakhov, V. Machining Simulation of Ti6Al4V Using Coupled Eulerian-Lagrangian Approach and a Constitutive Model Considering the State of Stress. *Simul. Model. Pract. Theory* **2021**, *110*, 102312. [CrossRef]
11. Calamaz, M. Approche Expérimentale et Numérique de l'Usinage à Sec de l'Alliage Aéronautique TA6V. Ph.D. Thesis, Institut Supérieur d'Ingénierie de la Conception, Bordeaux, France, 2008.
12. Zhen-Bin, H.; Komanduri, R. On a Thermomechanical Model of Shear Instability in Machining. *CIRP Ann. Manuf. Technol.* **1995**, *44*, 69–73. [CrossRef]
13. Davies, M.A.; Burns, T.J.; Evans, C.J. On the Dynamics of Chip Formation in Machining Hard Metals. *CIRP Ann. Manuf. Technol.* **1997**, *46*, 25–30. [CrossRef]
14. Xue, Q.; Meyers, M.A.; Nesterenko, V.F. Self-Organization of Shear Bands in Titanium and Ti–6Al–4V Alloy. *Acta Mater.* **2002**, *50*, 575–596. [CrossRef]
15. Grebe, H.A.; Pak, H.-R.; Meyers, M.A. Adiabatic Shear Localization in Titanium and Ti-6 Pct Al-4 Pct V Alloy. *Metall. Trans. A* **1985**, *16*, 761–775. [CrossRef]
16. Wan, Z.P.; Zhu, Y.E.; Liu, H.W.; Tang, Y. Microstructure Evolution of Adiabatic Shear Bands and Mechanisms of Saw-Tooth Chip Formation in Machining Ti6Al4V. *Mater. Sci. Eng. A* **2012**, *531*, 155–163. [CrossRef]
17. Rhim, S.-H.; Oh, S.-I. Prediction of Serrated Chip Formation in Metal Cutting Process with New Flow Stress Model for AISI 1045 Steel. *J. Mater. Process. Technol.* **2006**, *171*, 417–422. [CrossRef]
18. Calamaz, M.; Coupard, D.; Girot, F. A New Material Model for 2D Numerical Simulation of Serrated Chip Formation When Machining Titanium Alloy Ti–6Al–4V. *Int. J. Mach. Tools Manuf.* **2008**, *48*, 275–288. [CrossRef]
19. Chen, G.; Ge, J.; Lu, L.; Liu, J.; Ren, C. Mechanism of Ultra-High-Speed Cutting of Ti-6Al-4V Alloy Considering Time-Dependent Microstructure and Mechanical Behaviors. *Int. J. Adv. Manuf. Technol.* **2021**, *113*, 193–213. [CrossRef]
20. Liu, R.; Melkote, S.; Pucha, R.; Morehouse, J.; Man, X.; Marusich, T. An Enhanced Constitutive Material Model for Machining of Ti–6Al–4V Alloy. *J. Mater. Process. Technol.* **2013**, *213*, 2238–2246. [CrossRef]
21. Shang, X.; Cui, Z.; Fu, M.W. Dynamic Recrystallization Based Ductile Fracture Modeling in Hot Working of Metallic Materials. *Int. J. Plast.* **2017**, *95*, 105–122. [CrossRef]
22. Ducobu, F.; Rivière-Lorphèvre, E.; Filippi, E. Material Constitutive Model and Chip Separation Criterion Influence on the Modeling of Ti6Al4V Machining with Experimental Validation in Strictly Orthogonal Cutting Condition. *Int. J. Mech. Sci.* **2016**, *107*, 136–149. [CrossRef]
23. Atlati, S.; Haddag, B.; Nouari, M.; Zenasni, M. Analysis of a New Segmentation Intensity Ratio "SIR" to Characterize the Chip Segmentation Process in Machining Ductile Metals. *Int. J. Mach. Tools Manuf.* **2011**, *51*, 687–700. [CrossRef]
24. Kouadri, S.; Necib, K.; Atlati, S.; Haddag, B.; Nouari, M. Quantification of the Chip Segmentation in Metal Machining: Application to Machining the Aeronautical Aluminium Alloy AA2024-T351 with Cemented Carbide Tools WC-Co. *Int. J. Mach. Tools Manuf.* **2013**, *64*, 102–113. [CrossRef]
25. Astakhov, V.P.; Shvets, S. The Assessment of Plastic Deformation in Metal Cutting. *J. Mater. Process. Technol.* **2004**, *146*, 193–202. [CrossRef]
26. Iqbal, S.A.; Mativenga, P.T.; Sheikh, M.A. A Comparative Study of the Tool–Chip Contact Length in Turning of Two Engineering Alloys for a Wide Range of Cutting Speeds. *Int. J. Adv. Manuf. Technol.* **2009**, *42*, 30. [CrossRef]
27. Schulz, H.; Abele, E.; Sahm, A. Material Aspects of Chip Formation in HSC Machining. *CIRP Ann. Manuf. Technol.* **2001**, *50*, 45–48. [CrossRef]
28. Joshi, S.; Tewari, A.; Joshi, S. Influence of Preheating on Chip Segmentation and Microstructure in Orthogonal Machining of Ti6Al4V. *J. Manuf. Sci. Eng.* **2013**, *135*, 61017. [CrossRef]
29. Hua, J.; Shivpuri, R. Prediction of Chip Morphology and Segmentation during the Machining of Titanium Alloys. *J. Mater. Process. Technol.* **2004**, *150*, 124–133. [CrossRef]
30. Arısoy, Y.M.; Özel, T. Prediction of Machining Induced Microstructure in Ti–6Al–4V Alloy Using 3-D FE-Based Simulations: Effects of Tool Micro-Geometry, Coating and Cutting Conditions. *J. Mater. Process. Technol.* **2015**, *220*, 1–26. [CrossRef]
31. Pan, Z.; Liang, S.Y.; Garmestani, H.; Shih, D.S. Prediction of Machining-Induced Phase Transformation and Grain Growth of Ti-6Al-4 V Alloy. *Int. J. Adv. Manuf. Technol.* **2016**, *87*, 859–866. [CrossRef]
32. Wang, B.; Liu, Z. Shear Localization Sensitivity Analysis for Johnson–Cook Constitutive Parameters on Serrated Chips in High Speed Machining of Ti6Al4V. *Simul. Model. Pract. Theory* **2015**, *55*, 63–76. [CrossRef]
33. Sun, J.; Guo, Y.B. Material Flow Stress and Failure in Multiscale Machining Titanium Alloy Ti-6Al-4V. *Int. J. Adv. Manuf. Technol.* **2009**, *41*, 651–659. [CrossRef]
34. Kolmogorov, V.L.; Smirnov, S.V. The Restoration of the Margin of Metal Plasticity after Cold Deformation. *J. Mater. Process. Technol.* **1998**, *74*, 83–88. [CrossRef]
35. Smirnov, S.V. The Healing of Damage after the Plastic Deformation of Metals. *Frat. Integrità Strutt.* **2013**, *7*, 7–12. [CrossRef]

36. Haddag, B.; Atlati, S.; Nouari, M.; Zenasni, M. Analysis of the Heat Transfer at the Tool–Workpiece Interface in Machining: Determination of Heat Generation and Heat Transfer Coefficients. *Heat Mass Transf.* **2015**, *51*, 1355–1370. [CrossRef]
37. Komanduri, R.; Brown, R.H. On the Mechanics of Chip Segmentation in Machining. *J. Eng. Ind.* **1981**, *103*, 33–51. [CrossRef]